**Hydrology and
Earth System
Sciences
Discussions**

The turbidity behavior in an Amazon floodplain

E. Alcântara[1], E. Novo[1], J. Stech[1], J. Lorenzzetti[1], C. Barbosa[2], A. Assireu[1], and
A. Souza[2,3]

[1]Brazilian Institute for Space Research, Remote Sensing Division, P.O. Box 12227-010,
São José dos Campos, SP, Brazil
[2]Brazilian Institute for Space Research, Image Processing Division, P.O. Box 12227-010,
São José dos Campos, SP, Brazil
[3]ETEP Faculdades, P.O. Box 12242-800, São José dos Campos, SP, Brazil

HESSD

6, 3947–3992, 2009

**The turbidity
behavior in an
Amazon floodplain**

E. Alcântara et al.

Title Page

Abstract	Introduction
Conclusions	References
Tables	Figures

|◄ | ►|

◄ | ►

Back | Close

Full Screen / Esc

Printer-friendly Version

Interactive Discussion

Abstract

The main objective of this study is to understand the turbidity behavior of an Amazon Floodplain Lake. Observations of turbidity provide quantitative information about water quality. However, the number of available in situ measurements for water quality determination is usually limited in time and space. Here, we present an analysis of the temporal and spatial variability using two approaches: (i) the first is based on wavelet analysis of a turbidity time series measured by an automatic monitoring system; (ii) the second is based on turbidity samples measured in different locations and then interpolated by an ordinary kriging algorithm. The space/time turbidity variability is clearly related to the Amazon River flood pulses in the floodplain. When the water level in the floodplain is rising or receding, the exchange between the Amazon River and the floodplain is the major driving force in turbidity variability. At high water level, the turbidity variability is controlled by the lake bathymetry. Finally, when the water level is low, the wind action and lake morphometry are the main causes of turbidity variability. The combined use of temporal and spatial data showed a great potential for understanding the turbidity behavior in a complex aquatic system, like the Amazon floodplain.

1 Introduction

Turbidity is an important optical parameter in aquatic systems because it affects aquatic organisms at every level of the food chain, from microscopic algae to fish, by preventing sunlight penetrating the water column. Turbidity essentially depends on the amount of particulate material suspended in the water, which includes and is influenced by phytoplankton, sediments from erosions, re-suspended sediments from the bottom, waste discharge, algae growth and urban runoff (Han and Rundquist, 1998; Wetzel, 2001). Because the suspended particles absorb heat from the sunlight making turbid waters become warmer, and so reducing the concentration of dissolved oxygen in the water column is reduced (Kirk, 1983).

Turbidity is measured in nephelometric units (NTU), which refers to the type of instrument (turbidimeter or nephelometer) used for estimating light scattering from suspended particulate material. The well-known Secchi depth (visual technique which requires manually lowering a painted disk into the water) is the most common measure of turbidity (Wetzel, 2001). However, this parameter is hard to map in dynamic and complex environment such as floodplains, which periodically oscillates between terrestrial and aquatic phases (Junk, 1997). According to (Meade et al., 1985) floodplains play a major role in the storage of suspended solids transported from the Andes, with 80% of these suspended solids from the Amazon River corridor entering the floodplains being temporally deposited (Mertes et al., 1996).

The amount of suspended material in water masses is related to changes in flow and the resulting turbidity affects the zooplankton community (De Leo and Ferrari, 1993) as well as its composition (Wetzel, 2001) and phytoplankton production. It eliminates the most sensitive organisms (Miquelis et al., 1998) and modifies competition between zooplankton taxa (Wetzel, 2001).

Besides the actual level of turbidity, the duration of high turbidity events is also important. Very high levels of turbidity for a short period of time may not be significant and may even be less of a problematic than a lower level that persists longer (Newcombe and Jensen, 1996). Algal turbidity varies seasonally and with depth in a complex manner in response to physical, chemical and biological changes in the water body. Inorganic and detrital particles from the watershed vary largely in response to hydrological events such as storms (Stech and Lorenzzetti, 1992; Tundisi et al., 2004). Moreover, the suspended sediment concentration plays a major role in turbidity enhancement (Roozen et al., 2003).

The study of water quality in these environments has been based mostly on datasets obtained at different sites or along track lines occupied during cruises (Jerosch et al., 2006). Moreover, the number of in situ measurements of water quality is limited and especially the number of time series and of spatial maps of variables (Zhang et al., 2003; George, 1997; Dekker et al., 2002; Tyler et al., 2006) is scarce. To identify any

HESSD

6, 3947–3992, 2009

The turbidity behavior in an Amazon floodplain

E. Alcântara et al.

Title Page

Abstract Introduction

Conclusions References

Tables Figures

◄ ►

◄ ►

Back Close

Full Screen / Esc

Printer-friendly Version

Interactive Discussion

The turbidity behavior in an Amazon floodplain

E. Alcântara et al.

type of fast alteration suffered by systems variables (pulses), long term environmental time series of continuously collected data are fundamental to identifying and classifying pulses and determining their role in aquatic systems (Stech et al., 2006).

With the availability of time series and the sampling of variables at different places wavelet analysis (Meyers et al., 1993; Kumar and Foufoula-Georgiou, 1997) can be used to study the time localized frequency content of the signal. Geostatistics (Bellehumeur et al., 2000; Hedger et al., 2001) can be used to assess the spatial variability patterns of variables.

Using geostatistical methods (Bellehumeur et al., 2000; Isaaks and Srivastava, 1989; Goovaerts, 1997; Skøien et al., 2006) some authors show that during a hydrological cycle the turbidity distribution change because of water level dynamics, water flow regimes, wind intensity, precipitation regimes and hydrodynamics (Alcântara et al., 2008). Moreover, long-term high frequency time series of environmental variables are fundamental to identify and classify pulses or short-term variability in the data and to determine their impact in aquatic systems. Pulses are defined as any type of fast change suffered by the system variables (Stech et al., 2006). Ideally, time series of aquatic systems are collected by automatic stations with the capacity of autonomous monitoring of limnological and meteorological variables (Glasgow et al., 2004; Stech et al., 2006). With the installation of an associated telemetric link the constant surveillance provided by these systems makes it possible to rapidly detect changes and trends in critical indicators (Glasgow et al., 2004). The high frequency, complexity and volume of the data generated by those telemetric monitoring systems requires the use of efficient analytical tools such as wavelet analysis (Meyers et al., 1993).

Here we show that the combination of high resolution time series and spatial data allows for a better understanding of the turbidity dynamics in the Amazon floodplain. Based on this, in this paper the main objective is to map the spatial distribution of the turbidity along the hydrologic cycle and identify factors controlling its short time variability.

Full Screen / Esc

Printer-friendly Version

Interactive Discussion

2 Study site and background

The Curuai floodplain (Fig. 1) covers an area varying from 1340 to 2000 km^2 at the low and the high water levels, respectively; with a maximum volume reaching 9.3 km^3 (Martinez and Le-Toan, 2006). This floodplain, located 850 km from the Atlantic Ocean, near Óbidos city (Pará State, Brazil), is formed by "white" water lakes characterized by high concentration of suspended sediments, "black" water lakes with high concentration of dissolved organic matter and low concentration of sediments and "clear" water lakes fed by rainfall and rivers draining from the surrounding "Terra Firme" (higher elevation terrain with no significant flooding, Barbosa, 2005; Novo et al., 2006).

In early January (over the course of the 2001–2002 water year), the Amazon River dominated the mixture (64%). From this date until the beginning of April, the river water contribution slightly decreased while contributions from watersheds and direct rainfall increased. By mid-April water from rainfall constituted as much as 17% while contributions from local upland watershed and from watershed located in the aquatic-terrestrial transition zone reached their maxima by the end of February, constituted 14% and 15%, respectively. The groundwater reservoir contribution was highest at the end of December reaching 5% of the mixture (Bonnet et al., 2008).

The lakes are connected to each other and also to the Amazon River. The Curuai floodplain is controlled by the Amazon River flood pulse, which creates four water level stages in the floodplain-river system. Water storage in the floodplain starts between November and January and lasts until May–June. The drainage phase starts in July and lasts until November. The largest exported volume occurs from August to October. On an annual basis, the floodplain represents a source of water to the Amazon River (Bonnet et al., 2008).

The residence time of the riverine water within the floodplain is 5±0.8 month, while the residence time of water from all sources is 3±0.2 months (Bonnet et al., 2008). The lowest and highest absolute water levels recorded at the Curuaí gauging station during the 1982–2003 period were 3.03 m and 9.61 m, respectively.

Sediment accumulates in the floodplain from December to April, while during the low water stage; it is exported to the mainstream. The mean average sediment storage calculated for the floodplain varies between 558 and 828×10^3 t yr^{-1} (Maurice-Bourgoin et al., 2007). According to (Moreira-Turcq et al., 2004) the Curuai floodplain is a sediment accumulation system, with high rate of bottom deposition in some specific lakes (i.e. Santa Ninha Lake, 1 cm yr^{-1}). Of the influx of suspended material from the Amazon River into the floodplain, about 50% is deposited. The author (Amorim, 2006) shows that in general manner the suspended materials in the Curuai floodplain is composed mainly of silt and clay (Fig. 2).

The average annual precipitation in the Curuai floodplain is 2447 mm year^{-1} (Fig. 3), compared to average potential evaporation of 1400 mm year^{-1} (average obtained by a time series from 1990 to 2001), with the wet season lasting from January to June and a drier season from July to December (Barroux, 2006). These seasons modulate the water level dynamics in Curuai floodplain.

Another important parameter to turbidity generation in floodplain systems is water level dynamics (Roozen et al., 2003). The water level dynamics in Curuai floodplain is modulated by the water level near the Óbidos city (see Fig. 1) that characterizes the water level dynamics. A theoretical exchange of water between the floodplain and the Amazon River is shown in Fig. 4, based on (Barbosa, 2005).

Closer to the maximum water level in the floodplain, the exchange with the river is very low and the surface water circulation is caused mainly by wind (Alcântara et al., 2008). In the receding state the exchange of water between the river and the floodplain is reversed, i.e., there is a flux is from the floodplain to the river. When the water level drops to the lowest water level, the exchange of water between the river and the floodplain reaches its minimum. In summary, the floodplain stores water during the rising stage of the Amazon River and releases it when the river level is decreasing (Maurice-Bourgoin et al., 2007).

The rate of inundation is influenced by floodplain geomorphology (Mertes et al., 1995), density of floodplain channels and the ratio of local drainage basin area to lake

[HESSD](#)

6, 3947–3992, 2009

The turbidity behavior in an Amazon floodplain

E. Alcântara et al.

Title Page	
Abstract	Introduction
Conclusions	References
Tables	Figures

◄◄	►►
◄	►
Back	Close

Full Screen / Esc

Printer-friendly Version

Interactive Discussion

area (Lesack and Melack, 1995). The floodplain presents 93% of the flooded area between 2–6 m of depth (considering the water level reference of 936 cm). The deepest lake is the "Lago Grande" and the shallowest are the "Açaí" and Santa Ninha Lakes (Fig. 5). Almost 0.04% of the floodplain is below of the sea level (considering the mean altitude of 9 m in the floodplain in relation to sea level (Barbosa, 2005).

The circulation in the floodplain in beginning of December to the end of January is from west to east (Barbosa, 2005; Barroux, 2006). The main flow channels from the Amazon River to the Curuai floodplain are located in "Lago Grande" situated at east of floodplain, Lake "Salé" at northwest, and Lake "Santa Ninha" at northeast of floodplain (see Fig. 1 for location of Lakes). Also, at the low water level the main channel of "Lago Grande" is influenced by dynamic tide (Lima et al., 1995) and becomes the most important channel for water flow from Amazon River into the floodplain (Barroux, 2006).

3   In situ data

3.1   Temporal domain

The temporal variability of turbidity in the Curuai floodplain was studied using the data collected by an anchored buoy system named Environmental Monitoring System – SIMA (Fig. 6a). SIMA was developed by INPE and consists of an anchored buoy (see Fig. 1 for location) containing meteorological (atmospheric pressure, relative humidity, air temperature, wind direction and intensity, incoming and reflected solar radiation) and water quality (chlorophyll-a, pH, turbidity, dissolved oxygen, electric conductivity, nitrate, ammonia, water temperature, water flow direction and intensity) sensors (water quality YSI multi-parameter sonde and for meteorological from R. M. Young) supported by data storage systems, battery and the transmission antenna (Fig. 6a). The data are collected in preprogrammed time intervals (1 h) and are transmitted via satellite in quasi-real time to any user in a range of 2500 km from the acquisition point. In this work we analyzed the time series of turbidity measurements from 20 November 2004

to 26 April 2005 (Fig. 6b). The water depth at the SIMA location was approximately 5.5 m in high water level and 1.38 m in the low water regime (Alcântara, 2006).

3.2 Spatial domain

Turbidity measurements were carried out from 2003 to 2004 at several stations (see Fig. 7 for location) at specific Curuai floodplain lake water levels (Table 1) using a HORIBA U-10 multi-sensor probe.

This equipment provides turbidity measurements in NTU (Nephelometric Turbidity Unit) with a resolution of 1 NTU. The HORIBA calibration was performed for each day of sampling. Sampling locations were defined based on Thematic Mapper sensor image onboard Landsat-5 satellite acquired during similar floodplain stage (Barbosa, 2005). The period of sampling by HORIBA and SIMA is different because the SIMA was installed at the end of 2004. The distribution of turbidity samples through the Curuai floodplain (in standard deviation bins) are shown in Fig. 7.

4 Methodological approach

4.1 Time series analysis

4.1.1 Fourier power spectrum

The turbidity time series was analyzed using the Fourier power spectrum. The function that implements the transform is given by:

$$X(k+1) = \sum_{N=0}^{N-1} x(n+1)W_N^{kn} \tag{1}$$

Where $Wn = e^{-j(\frac{2\pi}{N})}$, N is the number of points and X is the discrete Fast Fourier Transform of the turbidity time series.

When performing the periodogram estimate the effect of leakage is very common and data windowing is the solution to this problem (Press et al., 1992). Data windowing modifies the relationship between the spectral estimate at discrete frequencies and its continuous (periodogram) spectrum at nearby frequencies. There are many window functions used to prevent spectral leakage, most of them rising from zero to a peak and then falling again, in this work we use Hanning and Hamming windows. The first was used to prevent leakage while the last was used to smooth the resulting spectra. The Hanning and Hamming window coefficients are, respectively, given by:

$$w(n) = 0.5 \left\{ 1 - \cos \left[2\pi \frac{n}{N-1} \right] \right\}, n = 1...N \tag{2}$$

$$w(n) = 0.54 - 0.46 \cos \left[2\pi \frac{n}{N-1} \right], n = 1...N \tag{3}$$

The smoothing of the power spectrum is employed to reduce the variance and to increase statistical confidence, or reduce confidence limits. A compromise must be found between strong smoothing (more confidence but stronger bias) and weak smoothing (less confidence but less bias). In this work we run the smoothing using the Hamming window at a variable length. The inferior and superior confidence limits for the spectra area, respectively, given by:

$$CL_{\text{inf}} = \frac{df}{\left[\chi \left(df, \frac{a}{2} \right) \right]} \tag{4}$$

$$CL_{\text{inf}} = \frac{df}{\left[\chi \left(df, \frac{1-a}{2} \right) \right]} \tag{5}$$

Where χ is the Chi square distribution, df is the number of degrees of freedom, $a = 1 - p/100$ and p is the confidence level (95%).

The turbidity behavior in an Amazon floodplain

E. Alcântara et al.

Back | Close

Full Screen / Esc

Printer-friendly Version

Interactive Discussion

4.1.2 Wavelet analysis

The time frequency space of turbidity time series was analyzed using the wavelet transform. Wavelet analysis is becoming a common tool for analyzing localized variations of power within an environmental time series (Meyers et al., 1993; Kumar and Foufoula-Georgiou, 1997; Massei et al., 2006). Decomposing an environmental time series into time-frequency space allows for the determination of both the dominant modes of variability and how those modes vary in time.

We analyzed the turbidity time series obtained from SIMA data by continuous wavelet analysis using the Morlet wavelet as reference analyzing function (the so-called "mother wavelet"). The Morlet wavelet is the most common wavelet transform, which consists of a Gaussian-windowed complex sinusoid defined in the time and frequency domains by:

$$\psi_0(\eta) = \pi^{-\frac{1}{4}} e^{i\omega_0\eta} e^{-\frac{\eta^2}{2}} \tag{6}$$

Where ω_0 is the non-dimensional frequency, here taken to be 6 to satisfy the admissibility condition (Farge, 1992); η is a non-dimensional time parameter and $\psi_0(\eta)$ is the wavelet function.

Wavelet spectral power at different scale (ω) and time location (τ) can be calculated by:

$$P_w(\omega, \tau) = |W(\omega, \tau, x(t)|^2 \tag{7}$$

Where W is the wavelet transform described below.

The continuous wavelet transform of a discrete sequence x_n is defined as the convolution of x_n with a scaled and translated version of $\psi_0(\eta)$ (Torrence and Compo, 1998). The wavelet transform W for a given time series x is calculated by:

$$W_n^x(\omega) = \sqrt{\frac{\delta t}{\omega}} \sum_{k'=1}^{N} x_n \psi * \left[(k-n)\frac{\delta t}{\omega} \right] \tag{8}$$

Where * indicates the complex conjugate; δt is the uniform time step, k' is an integer from 1 to N (number of data points) and x_n is the time series data. The scale-averaged spectral-power-based wavelet analysis reflects the average variance for different time scales (frequency or period). The calculation procedures of continuous wavelet analy-
5 sis were coded in Matlab 6.5 (The MathWorks, Inc., Natick, MA).

4.1.3 Cross wavelet and coherence

To explain in more detail the importance of wind on turbidity time series evidenced by Alcântara et al. (2008, 2009) we apply the cross wavelet and wavelet coherence in these two time series (Maraun and Kurths, 2004). The cross wavelet transform
10 of two time series x_n and y_n is defined as $W^{xy}=W^{x}W^{y*}$, where * denotes complex conjugation, so the cross wavelet power could be defined as $\left|W^{xy}\right|$ (Grinsted et al., 2004). The interpretation of complex argument arg(W^{xy}) can be interpreted as the local relative phase between x_n and y_n in time frequency space. The cross wavelet power theoretical distribution of two time series with background power spectra P_k^x and
15 P_k^y is given in Torrence and Compo (1998) as:

$$D \left(\frac{\left| W_n^x(s) W_n^{y*}(s) \right|}{\sigma_x \sigma_y} < p \right) = \frac{Z_v(p)}{v} \sqrt{P_k^x P_k^y} \tag{9}$$

Where $Z_v(p)$ is the confidence level associated with the probability p for a pdf defined by the square root of the product of two χ^2 distributions. Cross wavelet power reveals areas with high common power.
20 Another useful measure is how coherent the cross wavelet is in time frequency space. The wavelet coherence could be defined following Torrence and Webster (1998)

as:

$$R_n^2(s) = \frac{\left| S\left(s^{-1} W_n^{wy}(s)\right) \right|^2}{S\left(s^{-1} \left| W_n^x(s)\right|^2\right) . S\left(s^{-1} \left| W_n^y(s)\right|^2\right)} \tag{10}$$

Where S is a smoothing operator. Notice that this definition closely resembles that of a traditional correlation coefficient, and is useful to think of the wavelet coherence as a localized correlation coefficient in time frequency space. The calculation procedures of cross wavelet and wavelet coherence were coded in Matlab 6.5 (The MathWorks, Inc., Natick, MA).

The high frequency turbidity time series have made it possible the study of bottom resuspension episodes that cause turbidity increases. Particularly in shallow lakes, the effects of wind inducing sediment resuspension have been shown (Booth et al., 2000). These wind-induced physical processes are important for sediment transport and can be the dominant (Lou et al., 2000). We applied a method (Booth et al., 2000) for predicting the wind-induced bottom resuspension in the SIMA location during the low water stage.

4.1.4 Predicting bottom resuspension events from wind-induced waves

Wind speed was measured by SIMA at 3 m above the water surface (Fig. 6), and the data were normalized to 10 m height (Fig. 8a) using (Justus and Mikhail, 1976):

$$U_{10} = U_z \left(\frac{z}{z_a}\right)^n \tag{11}$$

Where U_{10} is the wind velocity (m s^{-1}) at 10 m height U_z is the wind velocity measured by SIMA at height z, z_a is the height where the anemometer measures the wind velocity

(3 m) and n is:

$$n = \left[\frac{0.37 - 0.088 \ln U_z}{1 - 0.088 \ln \left(\frac{z_a}{10} \right)} \right] \tag{12}$$

Wind action at the surface of the lake injects energy into the water column and thus generates surface and internal waves as well as mean circulation and turbulence, all of which can lead to vertical mixing (Stevens and Imberger, 1996). The minimum wind velocity (critical windspeed, U_c) needed to generate wave action reaching the bottom sediment was calculated according to (Booth et al., 2000):

$$U_c = \left\{ 1.2 \left[4127 \left(\frac{T_c^3}{F} \right) \right]^{0.813} \right\} \tag{13}$$

Where U_c is the critical wind speed (in m s^{-1}); T_c is the critical wave period and F is the effective fetch (in m) calculated according to (Carper and Bachmann, 1984).

The basic assumption of this simple model is that the effect of waves is felt down to a depth of approximately $\frac{L}{2}$, where L is the wavelength of the surface waves. So, if the water depth (d) is less than $\frac{L}{2}$ there is a wave energy transfer to the bottom sediments that can result in sediment resuspension.

The critical wave period (T_c) is given by (CERC, 1984):

$$T_c = \left(\frac{4\pi d}{g} \right)^{\frac{1}{2}} \tag{14}$$

The turbidity behavior in an Amazon floodplain

E. Alcântara et al.

Title Page

Abstract | Introduction

Conclusions | References

Tables | Figures

|◄ | ►|

◄ | ►

Back | Close

Full Screen / Esc

Printer-friendly Version

Interactive Discussion

4.2 The spatial domain

4.2.1 Ordinary Kriging algorithm

Geostatistics is focused on the spatial context and the spatial relationships present in the data. It provides tools for quantification and exploitation of spatial autocorrelation, and algorithms for data interpolation and uncertainty quantification (Isaaks and Srivastava, 1989; Goovaerts, 1997). The autocorrelation structure is used to estimate the variable values at points not sampled in the field (Bellehumeur et al., 2000). A central aspect of geostatistics is the use of spatial autocovariance structures, often represented by the (semi)variogram, or its cousin the autocovariogram, which differentiate different kinds of spatial variability (Burrough, 2001).

We used the ordinary kriging algorithm to interpolate in situ turbidity measurements into a turbidity map. The calculation of the Kriging weights is based upon the estimation of a semivariogram model, described as:

$$\gamma(h) = \frac{1}{2}Var[z(s+h) - z(s)] \tag{15}$$

Where: $\gamma(h)$ is an estimated value of the semivariance for lag h. The estimation of a semivariogram model relies on two important assumptions: the quantity $\gamma(h)$ exists and is finite for all choices of h and s, and that it does not depend on s. The ordinary kriging estimator is:

$$Z(x,y) = \sum_{i=1}^{n} w_i z_i \tag{16}$$

Where n is the number of measurements, z_i are the corresponding attributes values, and w_i are the weights (Isaaks and Srivastava, 1989).

The semivariogram was fitted with several theoretical models (spherical, exponential, Gaussian, linear and power) using the weighted least square method. The theoretical model that gives minimum standard error was chosen for further analysis.

The turbidity behavior in an Amazon floodplain

E. Alcântara et al.

Theoretical semivariogram models employ three main coefficients scaling the fit to experimental semivariograms: (i) *range* is a measurement of the curve's horizontal scale and corresponds to the maximum distance of spatial dependence; (ii) *nugget effect* is the y-intercept height and corresponds to a residual variation at the shortest sampling interval, random and not spatially correlated; (iii) *sill* is the remaining height of the curve above its y-intercept (nugget), and corresponds to the variance due to spatial structure (Isaaks and Srivastava, 1989).

Semivariogram models often have different ranges and/or sills in different directions. For the case where only the range changes with direction, the anisotropy is known as geometric anisotropy If only the sill changes with direction, the anisotropy is known as zonal anisotropy. The anisotropy modeling (Isaaks and Srivastava, 1989) usually starts with determining the anisotropy axes by experimentally determining the directions corresponding to the minimum and maximum range or sill. The parameters used to realize the interpolation to turbidity samples in each water level are in summarized in Table 2.

The equations representing the fitting models used to interpolate the turbidity distribution during rising (Eq. 17), high (Eq. 18), receding (Eq. 19) and low (Eq. 20) water levels are:

$$\gamma(h) = 619 + 114\left[\text{Gau}\left(\sqrt{\left(\frac{h_{94°}}{\varepsilon}\right)^2 + \left(\frac{h_{216°}}{16\,436}\right)^2}\right)\right] + 7770\left[\text{Gau}\left(\sqrt{\left(\frac{h_{94°}}{17\,924}\right)^2 + \left(\frac{h_{216°}}{16\,436}\right)^2}\right)\right] \quad (17)$$

$$+ 1480\left[\text{Gau}\left(\sqrt{\left(\frac{h_{94°}}{17\,924}\right)^2 + \left(\frac{h_{216°}}{\infty}\right)^2}\right)\right]$$

$$\gamma(h) = 4.98 + 20.45\left[\text{Gau}\left(\sqrt{\left(\frac{h_{100°}}{\varepsilon}\right)^2 + \left(\frac{h_{233°}}{14\,637}\right)^2}\right)\right] + 119.64\left[\text{Gau}\left(\sqrt{\left(\frac{h_{100°}}{12\,003}\right)^2 + \left(\frac{h_{233°}}{14\,637}\right)^2}\right)\right] \quad (18)$$

$$+ 8.2\left[\text{Gau}\left(\sqrt{\left(\frac{h_{100°}}{12\,003}\right)^2 + \left(\frac{h_{233°}}{\infty}\right)^2}\right)\right]$$

The turbidity behavior in an Amazon floodplain

E. Alcântara et al.

Full Screen / Esc

Printer-friendly Version

Interactive Discussion

The turbidity behavior in an Amazon floodplain

E. Alcântara et al.

$$\gamma(h) = 401 + 229\left[\mathrm{Exp}\left(\sqrt{\left(\frac{h_{94°}}{\varepsilon}\right)^2 + \left(\frac{h_{216°}}{12\,402}\right)^2}\right)\right] + 3567\left[\mathrm{Exp}\left(\sqrt{\left(\frac{h_{94°}}{16\,424}\right)^2 + \left(\frac{h_{216°}}{12\,402}\right)^2}\right)\right] \quad (19)$$

$$+ 261\left[\mathrm{Exp}\left(\sqrt{\left(\frac{h_{94°}}{16\,424}\right)^2 + \left(\frac{h_{216°}}{\infty}\right)^2}\right)\right]$$

$$\gamma(h) = 8420 + 7140\left[\mathrm{Gau}\left(\sqrt{\left(\frac{h_{94°}}{\varepsilon}\right)^2 + \left(\frac{h_{216°}}{6140}\right)^2}\right)\right] + 66\,885\left[\mathrm{Gau}\left(\sqrt{\left(\frac{h_{94°}}{9379}\right)^2 + \left(\frac{h_{216°}}{6140}\right)^2}\right)\right] \quad (20)$$

$$+ 10\,430\left[\mathrm{Gau}\left(\sqrt{\left(\frac{h_{94°}}{9379}\right)^2 + \left(\frac{h_{216°}}{\infty}\right)^2}\right)\right]$$

Where $\gamma(h)$ is the semivariance at lag h, $h_{n°}$ is the semivariance due to angles of anisotropy, ε is the range for the lower anisotropy angle. Gau and Exp are the Gaussian and Exponential models, respectively.

5 Results and discussion

5.1 Time series analysis

The time series of turbidity collected by SIMA consists of 3764 hourly samples (standard deviation of ±176.5 NTU) with a minimum, mean and maximum of 1.6, 126.9 and 1091 NTU, respectively.

Before analyze the variability of turbidity time series we will characterize and summarize their time dependence. The highest values of turbidity occur from November to half of December 2004 and decrease from second half of December to April 2005. Moreover, the smallest values occur from March to April 2005 (see Fig. 8).

The Fig. 8 shows also the time dependence $f(t)$ of turbidity by an eight-term Gaussian series:

$$f(t) = 386.6 \exp\left(-\left(\frac{t-106}{44.57}\right)^2\right) + 642.3 \exp\left(-\left(\frac{t-308.7}{91.08}\right)^2\right) + (-428.2)\exp\left(-\left(\frac{t-317.9}{35.99}\right)^2\right) + \quad (21)$$

$$486.2 \exp\left(-\left(\frac{t-35.87}{105.2}\right)^2\right) + 102.4 \exp\left(-\left(\frac{t-802.5}{32.56}\right)^2\right) + 80.17 \exp\left(-\left(\frac{t-1571}{85.59}\right)^2\right) +$$

$$456 \exp\left(-\left(\frac{t-187}{33.91}\right)^2\right) + 87.4 \exp\left(-\left(\frac{t-1485}{2277}\right)^2\right)$$

Due to high variability found during November and December the model fitting did not capture all the variability. This could be see in Fig. 8b where the residuals is more high during this period. From the second half of December to April the fitting work very well. The overall fitting was R^2=0,94 (p=0.05 and RMSE=36.18). This pattern of variability will be analyzed by Fourier and wavelet analysis.

In general the time series of turbidity shows a response to flood pulses in Curuai floodplain (Alcântara, 2006). The highest values of turbidity occurred in the low water level regime, which can be attributed to sediment resuspension events generated by waves at sufficiently high wind intensity. To characterize the main periods of variability of the whole time series a Fourier power spectrum will be applied.

The Fourier power spectrum show that for until 100 h (from 20 to 24 November 2004) the power density is small and noised and still increasing the power. From 100 to 150 h have an increase of power (from 24 to 26 November 2004). A second peak occurs in 480 h (10 December 2005) and the third in 630 h (16 December 2005). From this point the power energy is constant (Fig. 9).

All this peaks occur from November 2004 to December 2005. This occurs due to high variability of turbidity during this period (Fig. 8). This is a global analysis of power energy and for a localized time-frequency space analysis a wavelet analysis will be making.

The turbidity behavior in an Amazon floodplain

E. Alcântara et al.

Title Page

Abstract | Introduction

Conclusions | References

Tables | Figures

◄ | ►

◄ | ►

Back | Close

Full Screen / Esc

Printer-friendly Version

Interactive Discussion

The wavelet analysis show in Fig. 10 reveal that in November 2004 the period of high variability is from 8 to 512 h (∼21 days), below this the periods is not significant at 95% confidence level (separated by the cone of influence). To December 2004 the periods increase until 2048 h (∼85 days), with peaks in the end of this month be-

5   tween 16–64 h (∼2 days). From January to February 2005 the period increases until 4096 h (∼170 days). From March to April 2005 the periods increase again until 1024 h (42 days) without periods smaller than 128 h (∼5 days).

In fact the short periods showing in November and December 2004 is due to high variability of turbidity events. And in other hand the greater periods from January to

10   April 2005 is due to small variations in turbidity events.

The high mean values and standard deviation of turbidity in the low water level regime are caused mainly by wind action. In Curuai floodplain the wind speed can reach $10\,\mathrm{m\,s^{-1}}$ (see Fig. 11). The wind stress induces an energetic wave-affected layer in which both large-scale orbital movements and the dissipated turbulent energy

15   are important. The proximity of the surface and bottom boundaries in shallow lakes often generates a completely mixed water column during the resuspension events (Booth et al., 2000; Cózar et al., 2005). During the observational period winds acquired by SIMA at "Lago Grande" varied from 0.2 to $10\,\mathrm{m\,s^{-1}}$ with a preferential direction from southeast to northwest (Fig. 11).

20   To check the possibility of cause sediment resuspension during the low water level (November, December and January) we will apply the critical wave period (CERC, 1984). Our analysis of the suitability of wind to cause resuspension in the high water level was supported by (Novo et al., 2006) who show a rate less than $0.2\,\mathrm{cm\,h^{-1}}$ of water level change.

25   We check this for November 2004, event E1, when the variability is more high than the other months of the whole time series; December 2004, event E2, when the variability is small than November and January 2005, event E3, where the peaks of variability is more feasible to separate due to a small events of high turbidity.

The first event E1 corresponds to low water level, the event E2 corresponds to the

Title Page

Abstract | Introduction

Conclusions | References

Tables | Figures

|◄ | ►|

◄ | ►

Back | Close

Full Screen / Esc

Printer-friendly Version

Interactive Discussion

flow of water from the floodplain to the Amazon River; and the event E3 takes place when the water level begins to rise in response to the water flowing into the floodplain from the Amazon River.

The events E1, E2 and E3 can probably be attributed to the combination of high wind intensity and the shallow water level. In agreement to (Carper and Bachmann, 1984) the surface waves produced when wind blows across surface water cause the bottom resuspension and temporarily increase the turbidity.

The event E1 has a minimum, mean and maximum wind velocity of 2.75, 5.47 and 9.02 m s^{-1} and preferential wind direction from northwest to southeast (Fig. 12a). The event E2 has a minimum, mean and maximum wind velocity of 1.98, 4.5 and 5.75 m s^{-1}, with a preferential wind direction from northwest to southeast, during 24-h (Fig. 12b). The E3 has a minimum, mean and maximum wind velocity of 0.34, 2.37 and 5.95 m s^{-1}, with a preferential wind direction from northeast to southwest, during 24-h (Fig. 12c).

The critical windspeed (m s^{-1}) for event E1 is 0.44 and 1.04 (m s^{-1}) for E2 (Table 3). For event E3 the critical wind speed is 1.14 (m s^{-1}). Wind speeds above these values make suitable the bottom resuspension in the SIMA location. In both, E1 and E2 is suitable for the wind-induced bottom resuspension.

In the event E1 with peak of high turbidity and low turbidity marks an incident of unusually low turbidity in the low water level, in spite of the wind speed being above the critical threshold at which sediment resuspension can occur. However, due to the duration of the minimum wind speed (2.75 m s^{-1}) registered by SIMA is low when compared with the time series in this water stage. As a consequence a decantation of suspended solids occurs due to the end of the wind action in the surface water.

In accordance to (Moreira-Turcq et al., 2004) the silt and clay dominate the suspended solids in Curuai floodplain (87–98%), and at the end of wind action and the decrease of the current velocity would cause particle settling. In the low water stage the depositional processes in lakes and channels are disrupted by the wind induced resuspension of sediments (Maurice-Bourgoin, 2007) and bioturbation in shallow lakes (Maia et al., 2008).

To investigate this relationship we use a cross-wavelet analysis and coherence will apply to register the importance of wind action on turbidity behavior. Wavelet coherency is a measure of the intensity of the covariance of the two time series in time-frequency space, unlike the cross-wavelet power that is a measure of the common power.

5.2 Cross wavelet spectrum and wavelet coherence and phase

In Fig. 13a and b we present the cross-wavelet spectrum and coherency spectrum, respectively. Horizontal arrows indicate a simple linear relationship between turbidity and wind action. Arrows pointing to the right mean correlation (in phase) and an anticorrelation (in antiphase) is indicated by a left pointing arrow. Non-horizontal arrows refer to a more complicated (non-linear) phase difference (Valdés-Galicia and Velasco, 2008).

The cross wavelet spectrum between turbidity and wind intensity time series shows a high agreement in the first 500 h (∼20 days, from 20 November 2004 to 10 December 2005) for periods from 4 to 200 h (∼8 days) see Fig. 13a. These results confirm our results about the importance of wind action on surface water to enhance the turbidity during the low water level.

The coherence is high for this first 500 h mainly in periods of 4, 8 and 19 h. This coherence in low time frequency is due to sediment ressuspension caused by wind shown in Table 3 (Fig. 13b). The arrows presented in these periods are non-horizontal, that represent a complicated, non-linear, phase difference.

The agreement between turbidity and wind decreases with the raising water level when the wind does not cause sediment resuspension any more. As pointed out by Alcântara (2006) in high water level the turbidity values are low due to fine sediment decantation (see Fig. 2). So the high agreement migrate for higher periods (Fig. 13a) following the water level dynamics (see Fig. 4). And the coherence migrates too (Fig. 13b). This influences of wind action and water level dynamics influenced not only the time series domain but also in whole lake.

In order to investigate differences in turbidity between the various lakes in the Curuai

The turbidity behavior in an Amazon floodplain

E. Alcântara et al.

floodplain, the spatial turbidity distribution over the entire floodplain is determined by applying the ordinary kriging on turbidity collected in situ by a HORIBA U-10 multi-sensor.

5.3 Spatial analysis

5 Using a scatterplot the performance of ordinary kriging to interpolate the in situ turbidity data was evaluated for each sampling campaign (Fig. 14). The performance of all interpolated in situ turbidity data was statistically satisfactory and reliable. The most accurate interpolation was the one made for the data in the high water level regime (RMSE=3 NTU), while the interpolation for the low water level regime was the least
10 accurate (RMSE=25 NTU).

This is a result of the water level stability and low standard deviation in the high water level regime (mean=31.46, see Fig. 7d), and the high standard deviation (mean=771.11, see Fig. 7b) and sediment resuspension events in the low water level regime (see Table 3).

15 All in situ turbidity data were interpolated using the ordinary kriging algorithm to assess the turbidity distribution and variability in response to flood pulses (Fig. 15). According to (Bonnet et al., 2008) the water storage within the floodplain started between December and February, and lasted until June. From this time until the end of the water year, water was exported from the floodplain into the river, with the maximum
20 water export occurring from August to September.

The semivariogram for turbidity data during rising, high and low water level was best described by a Gaussian model, indicating a smoothly varying pattern in turbidity distribution. During receding water level the semivariogram was best represented by an exponential function, suggesting a dataset with a spatial pattern characterized by gradual
25 transition among several patterns interfering with each other (Burrough and Mcdonnell, 1998), see Table 2.

In the rising water level regime (Fig. 15a), the flow from the Amazon River to the Curuai floodplain starts in a channel located at the eastern border of the lake, then

migrating to small channels at the northwestern border (Alcântara et al., 2009). The yellow circle 1 marks a region of high turbidity formed by the water from the Amazon River entering through the channel located at the eastern border. The region of high turbidity marked by the yellow circle 2 was formed by water entering through the small channels located on the northwestern side. The yellow circle 3 marks a region of low turbidity, which is explained by the existence of a natural barrier as explained above (see Fig. 5).

In the high water level regime (Fig. 15b) the input of water from Amazon River is lowest and the turbidity tends to be spatially homogeneous (Alcântara et al., 2008). The areas of high turbidity (marked 1 and 2) correspond to the small channels connecting the floodplain with the Amazon River. Area 3 also corresponds to a connecting channel, however the turbidity is low. This occurs probably because this channel is the first to cease water input to the floodplain. Area 4 has a low turbidity due to the forest cover favoring a decrease in flow velocity and particle settling (mainly clay and silt, see Fig. 2) because of lower hydrodynamics.

In the receding water level regime (Fig. 15c) the preferential direction of flow is from west to east (Barbosa, 2005). As a result, the regions marked 1 and 2 in Fig. 12c show a high turbidity due to the friction of water at the channel borders. The high turbidity in area 3 stems from suspended solids entering from the east channel connected to the Amazon River. The receding water level stage causes a condition of turbulent flow, leading to increased turbulence.

In the low water level regime (Fig. 15d), exchange between the Amazon River and the Curuai floodplain reaches a minimum and the turbidity variability is mainly wind-driven. As discussed above, the preferential wind direction is from southeast to northwest (Fig. 11), causing water to pile up and generate a dowelling near the channel margins and an upwelling in the opposite direction. These regions are marked by the yellow circles 1 and 2.

6   Conclusions

This result shows the importance of high frequency and spatial data in limnological studies in aquatic complex systems (i.e. Amazon floodplain) in contrast to conventional studies with only occasional sampling can lead to misinterpretation of the turbidity behavior.

1. The flood pulse that occurs with the rising waters of the Amazon flood introduces turbidity from 80 to 180 NTU. The wind effect at low water stirring up the bottom sediments leads to turbidities exceeding 1100 NTU. Therefore, the highest turbidities and the greatest variability are caused by wind blowing over shallow water. Major re-suspension of sediment due to wind occurs and produces turbidity far greater than the initial turbid waters entering the lakes.

2. The analysis of turbidity samples spatially distributed with ordinary kriging algorithm showed the same dependence observed in the time series.

3. Ordinary kriging maps show the spatial distribution of high turbidity in the floodplain for the different water level regimes. At low water level, wind stress is the main driving force generating a high turbidity in the Curuai floodplain.

4. Wavelet analysis of the turbidity time series from a moored station gives insight the duration of re-suspension events due to wind, typically lasting 3 to 6 days.

Clearly, the integration of spatial-temporal data has a great potential for understanding the turbidity dynamics in a complex aquatic system such as the Amazon floodplain.

References

Alcântara, E. H.: Analysis of turbidity in Curuai floodplain through the integration of telemetric and MODIS/Terra image data (MSc. Dissertation), INPE: São José dos Campos, Brazil, 220 pp., 2006 (in Portuguese).

Alcântara, E. H., Stech, J. L., Novo, E. M. L. M., Shimabukuro, Y. E., and Barbosa, C. C. F.: Turbidity in the Amazon floodplain assessed through a spatial regression model applied to fraction images derived from MODIS/Terra, IEEE T. Geosci. Remote, 46, 2895–2905, 2008.

Alcântara, E. H., Barbosa, C. C. F., Stech, J. L., Novo, E. M. L. M., and Shimabukuro, Y. E.: Improving the spectral unmixing algorithm to map water turbidity distributions, Environ. Modell. Softw., 24, 1051–1061, 2009.

Amorim, M. A.: Study of early sedimentation in "Lago Grande de Curuai" várzea, Pará State, Brazil (MSc. Dissertation), UFF: Niterói, Brazil, 144 pp., 2006 (in Portuguese).

Barbosa, C. C. F.: Sensoriamento remoto da dinâmica de circulação da água do sistema planície de Curuai/ Rio Amazonas (PhD. Thesis), INPE: São José dos Campos, Brazil, 255 pp., 2005.

Barroux, G.: Bio-geochemical study of a lake system from the Amazonian floodplain: the case of "Lago Grande de Curuaí", Pará-Brazil (PhD Thesis), UPS: Toulouse, Frech, 304 pp., 2006 (in French).

Bellehumeur, C., Marcotte, D., and Legendre, P.: Estimation of regionalized phenomena by geostatistical methods: lake acidity on the Canadian Shield, Environ. Geol., 39, 211–220, 2000.

Bonnet, M. P., Barroux, G., Martinez, J. M., Seyler, F., Moreira-Turcq, P., Cochonneau, G., Melack, J. M., Boaventura, G., Maurice-Bourgoin, L., León, J. G., Roux, E., Calmant, S., Kosuth, P., Guyot, J. L., and Seyler, P.: Floodplain hydrology in an Amazon floodplain lake (Lago Grande de Curuaí), J. Hydrol., 349, 18–30, 2008.

Booth, J. G., Miller, R. L., McKee, B. A., and Leathers, R. A.: Wind-induced bottom sediment resuspension in a microtidal coastal environment, Cont. Shelf Res., 20, 785–806, 2000.

Title Page	
Abstract	Introduction
Conclusions	References
Tables	Figures
◄◄	►►
◄	►
Back	Close
Full Screen / Esc	
Printer-friendly Version	
Interactive Discussion	

Burrough, P. A.: GIS and Geostatistics: Essential partners for spatial analysis. Environ. Ecol. Stat., 8, 361–377, 2001.

Burrough, P. A. and Mcdonnell, R. A.: Principles of geographical information systems, 2rd Ed., Oxford University Press, New York, USA, 356 pp., 1998.

Carper, G. L. and Bachmann, R. W.: Wind resuspension of sediments in a prairie lake, Can. J. Fish. Aquat. Sci., 41, 1763–1767, 1984.

CERC: Shore protection manual, 1rd Ed., US Army Coastal Engineering Center, Viksburg, USA, 603 pp., 1984.

Cózar, A., Gálvez, J. A., Hull, V., García, C. M., and Loiselle, S. A.: Sediment resuspension by Wind in a shallow lake of Esteros Del Iberá (Argentina): a model based on turbidimetry, Ecol. Modell., 186, 63–76, 2005.

De Leo, G. A. and Ferrari, I.: Disturbance and diversity in a river zooplankton community: a neutral model analysis, Coenoses, 8, 121–129, 1993.

Dekker, A. G., Vos, R. J., and Peters, S. W. M.: Analytical algorithms for lake water TSM estimation for retrospective analyses of TM and SPOT sensor data, Int. J. Remote Sens., 23, 15–35, 2002.

Farge, M.: Wavelet transforms and their applications to turbulence, Annu. Rev. Fluid Mech., 24, 395–457, 1992.

Goovaerts, P.: Geostatistics for natural resources evaluation, Oxford University Press, New York, USA, 483 pp., 1997.

Glasgow, H. B., Burkholder, J. M., Reed, R. E., Lewitus, A. J., and Kleinmann, J. E.: Real-time remote monitoring of water quality: a review of current applications, and advancements in sensor, telemetry, and computing technologies, J. Exp. Mar. Biol. Ecol., 300, 409–448, 2004.

George, D. G.: The airborne remote sensing of phytoplankton chlorophyll in the lakes and tarns of the English Lake District, Int. J. Remote Sens., 18, 1961–1975, 1997.

Han, L. and Rundquist, D. C.: The impact of a wind-roughened water surface on remote measurements of turbidity, Int. J. Remote Sens., 19, 195–201, 1998.

Hedger, R. D., Atkinson, P. M., and Malthus, T. J.: Optimizing sampling strategies for estimating mean water quality in lakes using geostatistical techniques with remote sensing, Lakes and Reservoirs, Res. Manage., 6, 279–288, 2001.

Isaaks, E. H. and Srivastava, M. R.: An introduction to applied geostatistics, Oxford University Press, New York, USA, 561 pp., 1989.

Jerosch, K., Schlüter, M., and Pesch, R.: Spatial analysis of marine categories information us-

ing indicator Kriging applied to georeferenced video mosaics of the deep-sea Håkon Mosby Mud Volcano, Ecol. Info., 1, 391–406, 2006.

Junk, W. J.: The Central Amazon Floodplain: ecology of a pulsing system, 1rd Ed., Springer Verlag, Berlin, Germany, 525 pp., 1997.

5 Justus, C. G. and Mikhail, A.: Height variation of wind speed and wind distribution statistics, Geophys. Res. Lett., 3, 264–264, 1976.

Kirk, J. T. O.: Light and photosynthesis in aquatic environments, 1rd Ed., Cambridge University Press, Cambridge, USA, 401 pp., 1983.

Kumar, P. and Foufoula-Georgiou, E.: Wavelet analysis for geophysical application, Rev. Geo-
10 phys., 35, 385–412, 1997.

Lesack, L. F. W. and Melack, J. M.: Flooding hydrology and mixture dynamics of lake water derived from multiple sources in an Amazon floodplain lake, Water Resour. Res., 31, 329–345, 1995.

Lima, I. B. T., Carvalho, J. C., Ramos, F. M., Rosa, R. R., Sych, R. A., and Novo, E. L. M. M.:
15 Detecting climatic and tidal influence on the Amazon River level by wavelet analysis, Inter. Vere. Theor. Ang. Limn., 29, 1785–1788, 1995.

Lou, J., Schwab, D. J., Beletsky, D., and Hawley, N.: A model of sediment resuspension and transport dynamics in southern Lake Michigan, J. Geophys. Res., 105, 6591–6610, 2000.

Maia, P. D., Maurice, L., Cossa, D., Portugal, R. A., Etcheber, H., Souza, J. R., Guimarães, E.
20 M., and Boaventura, G. R.: Is the Curuai floodplain (Middle Amazon, Brazil) an efficient trap for particulate mercury?, Geophys. Res. (abstracts), 10, 12238, 2008.

Martinez, J.-M. and Le-Toan, T.: Mapping of flood dynamics and spatial distribution of vegeta-tion in the Amazon floodplain using multitemporal SAR data, Remote Sens. Environ., 108, 209–223, 2006.

25 Maraun, D. and Kurths, J.: Cross wavelet analysis: significance testing and pitfalls, Nonlin. Processes Geophys., 11, 505–514, 2004,
http://www.nonlin-processes-geophys.net/11/505/2004/.

May, C. L., Koseff, J. R., Lucas, L. V., Cloern, J. E., and Schoellhamer, D. H.: Effects of spatial and temporal variability of turbidity on phytoplankton blooms, Mar. Ecol. Prog. Ser., 254,
30 111–128, 2003.

Massei, N., Dupont, J. P., Mahler, B. J., Laignel, B., Fournier, M., Valdes, D., and Ogier, S.: Investigating transport properties and turbidity dynamics of a karst aquifer using correlation, spectral, and wavelet analyses, J. Hydrol., 329, 244–257, 2006.

The turbidity behavior in an Amazon floodplain

E. Alcântara et al.

Title Page

Abstract | Introduction

Conclusions | References

Tables | Figures

◀ | ▶

◀ | ▶

Back | Close

Full Screen / Esc

Printer-friendly Version

Interactive Discussion

Maurice-Bourgoin, L., Bonnet, M. P., Martinez, J. M., Kosuth, P., Cochonneau, G., Moreira-Turcq, P., Guyot, J. L., Vauchel, P., Filizola, N., and Seyler, P.: Temporal dynamics of water and sediment exchanges between the Curuaí floodplain and the Amazon River, Brazil, J. Hydrol., 335, 140–156, 2007.

5 Meade, R. H., Dunne, T., Richey, J. E., Santos, U. M., and Salati, E.: Storage and remobilization of suspended sediment in the lower Amazon River of Brazil, Science, 228, 488–490, 1985.

Moreira-Turcq, P. F., Jouanneau, B., Turcq, B., Seyler, P., Weber, O., and Guyot, J. L.: Carbon sedimentation at Lago Grande de Curuaí, a floodplain lake in the low Amazon region: insight into sedimentation rates, Palaeogeogr. Palaeocl., 214, 27–70, 2004.

10 Mertes, L. A. K., Daniel, D. L., Melack, J. M., Nelson, B., Martinelli, A., and Forsberg, B. R.: Spatial patterns of hydrology, geomorphology, and vegetation on the floodplain of the Amazon River in Brazil from a remote sensing perspective, Geomorphology, 13, 215–232, 1995.

Meyers, S. D., Kelly, B. G., and O'Brien, J. J.: An introduction to wavelet analysis in Oceanography and Meteorology: with application to the dispersion of Yanai Waves, Mon. Weather Rev., 121, 2858–2866, 1993.

15 Mertes, L. A. K., Dunne, T., and Martinelli, L. A.: Channel-floodplain geomorphylogy along the Solimões-Amazon River, Brazil, GSA Bulletin, 108, 1089–1107, 1996.

Miquelis, A., Rougier, C., and Pourriot, R.: Impact of turbulence and turbidity on the grazing rate of the rotifer Brachionus calyciflorus (Pallas), Hydrobiologia, 386, 203–211, 1998.

20 Newcombe, C. P. and Jensen, J. O. T.: Channel suspended sediment and fisheries: a synthesis for quantitative assessment of risk and impact, N. Am. J. Fish. Manage., 16, 693–727, 1996.

Novo, E. L. M. M., Barbosa, C. C. F., Freitas, R. M., Shimabukuro, Y. E., Melack, J. M., and Pereira-Filho, W.: Seasonal changes in chlorophyll distribution in Amazon floodplain lakes

25 derived from MODIS images, Limnology, 7, 153–161, 2006.

Press, W. H., Teukolsky, S. A., Vetterling, W. T., and Flannery, B. P.: Numerical recipes in fortran 77: the art of scientific computing, Vol. 1 of Fortran numerical recipes, Cambridge University Press, UK, 933 pp., 1992.

Roozen, F. C. J. M., Van-Geest, G. J., Ibelings, B. W., Roijackers, R., Scheffer, M., and Buijse,

30 A. D.: Lake age and water level affect the turbidity of floodplain lakes along the lower Rhine, Fresh. Bio., 48, 519–531, 2003.

Skøien, J. O., Merz, R., and Blöschl, G.: Top-kriging – geostatistics on stream networks, Hydrol. Earth Syst. Sci., 10, 277–287, 2006,

The turbidity behavior in an Amazon floodplain

E. Alcântara et al.

Title Page

Abstract	Introduction
Conclusions	References
Tables	Figures

|◄ | ►|

◄ | ►

Back | Close

Full Screen / Esc

Printer-friendly Version

Interactive Discussion

http://www.hydrol-earth-syst-sci.net/10/277/2006/.

Stech, J. L. and Lorenzzetti, J. A.: The response of the south Brazil bight to the passage of wintertime cold fronts, J. Geophys. Res., 97, 9507–9520, 1992.

Stech, J. L., Lima, I. B. T., Novo, E. M. L. M., Silva, C. M., Assireu, A. T., Lorenzzetti, J. A., Carvalho, J. C., Barbosa, C. C. F., and Rosa, R. R.: Telemetric Monitoring System for meteorological and limnological data acquisition, Verh. Internat. Verein. Limnol., 29, 1747–1750, 2006.

Stevens, C. and Imberger, J.: The initial response of a stratified lake to a surface shear stress, J. Fluid. Mech., 312, 39–66, 1996.

Tundisi, J. G., Matsumura-Tundisi, T., Arantes-Junior, J. D., Tundisi, J. E. M., Manzini, N. F., and Ducrot, R.: The response of Carlos Botelho (Lobo, Broa) reservoir to the passage of cold fronts as reflected by physical, chemical and biological variables, Braz. J. Bio., 64, 177–186, 2004.

Torrence, C. and Compo, G. P.: A Practical Guide to Wavelet Analysis, B. Am. Meteorol. Soc., 79, 61–78, 1998.

Torrence, C. and Webster, P.: Interdecadal changes in the ENSO-Monsoon system, J. Climate, 12, 2679–2690, 1999.

Tyler, A. N., Svab, E., Preston, E., Présing, M., and Kovács, W. A.: Remote sensing of the water quality of shallow lakes: A mixture modelling approach to quantifying phytoplankton in water characterized by high-suspended sediment, Int. J. Remote Sens., 27, 1521–1537, 2006.

Valdés-Galicia, J. F. and Velasco, V. M.: Variations of mid-term periodicities in solar activity physical phenomena, Adv. Space Res., 41, 297–305, 2008.

Wetzel, R. G.: Limnology – Lake and River Ecosystems, 3rd Ed., Academic Press: San Diego, USA, 1006 pp., 2001.

Zhang, Y., Pulliainen, J. T., Koponen, S. S., and Hallikainen, M. T.: Water quality retrievals from combined Landsat TM data and ERS-2 data in the Gulf of Finland, IEEE T. Geosci. Remote Sens., 41, 622–629, 2003.

The turbidity behavior in an Amazon floodplain

E. Alcântara et al.

Table 1. Descriptive statistics of the in situ turbidity data (NTU).

Water level regime	Period of sampling	Number of samples	Maximum value	Average value	Minimum value	Standard deviation
Receding water	23 Sep 2003 –9 Oct 2003	208	375	163.06	12	58.61
Low water	19 Nov 2003 –1 Dec 2003	202	1645	777.10	39	306.14
Rising water	1 Feb 2004 –14 Feb 2004	221	569	232.29	101	84.61
High water	31 May 2004 –21 Jun 2004	256	127	31.46	5	17.16

Table 2. Semivariogram parameters used to interpolate the turbidity.

Water level	direction Anisotropy	Structure	Nugget	Sill	>range	<range	Model
Rising	94°	1°	619	114	16 436	ε	Gaussian
		2°		7770	17 924	16 436	
		3°		1480	∞	17 924	
High	100°	1°	4.98	20.45	14 637	ε	Gaussian
		2°		119.64	14 637	12 003	
		3°		8.2	∞	12 003	
Receding	94°	1°	401	229	12 402	ε	Exponential
		2°		3567	16 424	12 402	
		3°		261	∞	16 242	
Low	94°	1°	8420	63 595	9379	ε	Gaussian
		2°		66 885	9379	6140	
		3°		10 430	∞	9379	

The turbidity behavior in an Amazon floodplain

E. Alcântara et al.

Table 3. Critical windspeed ($m\,s^{-1}$) limits to cause bottom sediment resuspension.

Depth (m)	Events	Fetch (m)	Uc ($m\,s^{-1}$)
1.38	E1	33 000	0.44
1.60	E2	11 556	1.04
2.32	E3	10 300	1.14

E. Alcântara et al.

Title Page

Abstract | Introduction

Conclusions | References

Tables | Figures

|◀ | ▶|

◀ | ▶

Back | Close

Full Screen / Esc

Printer-friendly Version

Interactive Discussion
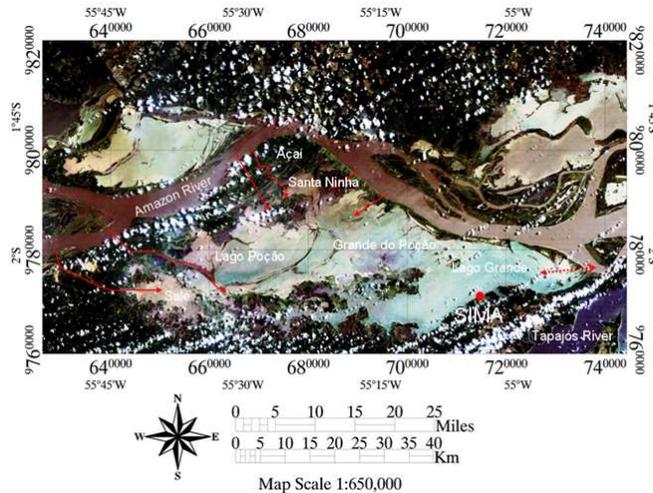
Fig. 1. (a) Location of Legal Amazon in Brazil, **(b)** Legal Amazon limits, and **(c)** Location of Curuai Floodplain (Pará State, Brazil) and the location of the automatic environmental data collection buoy system SIMA at "Lago Grande". The arrows indicate the main channels of connection Amazon River-floodplain.
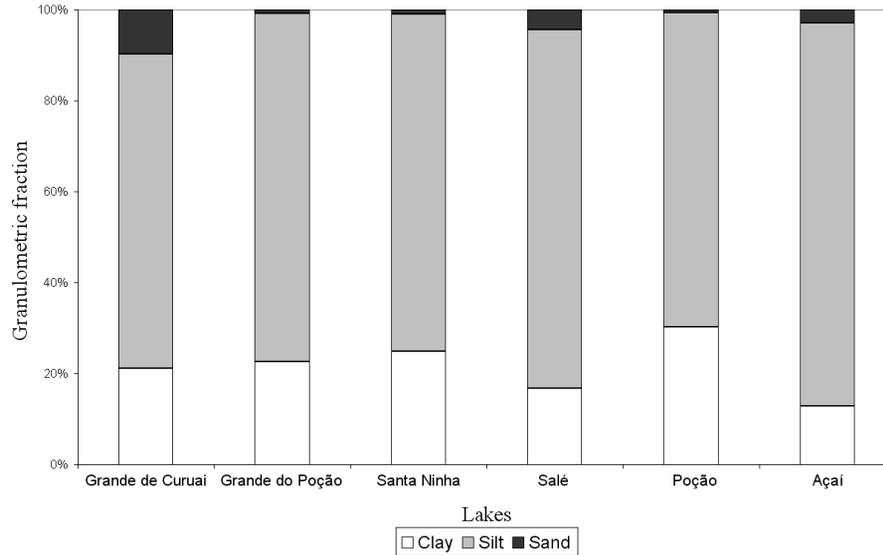
Fig. 2. Average values of granulometric fractions for each Curuai floodplain lakes (from Amorim, 2006).

E. Alcântara et al.

Title Page

Abstract   Introduction

Conclusions   References

Tables   Figures

◄   ►►

◄   ►

Back   Close

Full Screen / Esc

Printer-friendly Version

Interactive Discussion
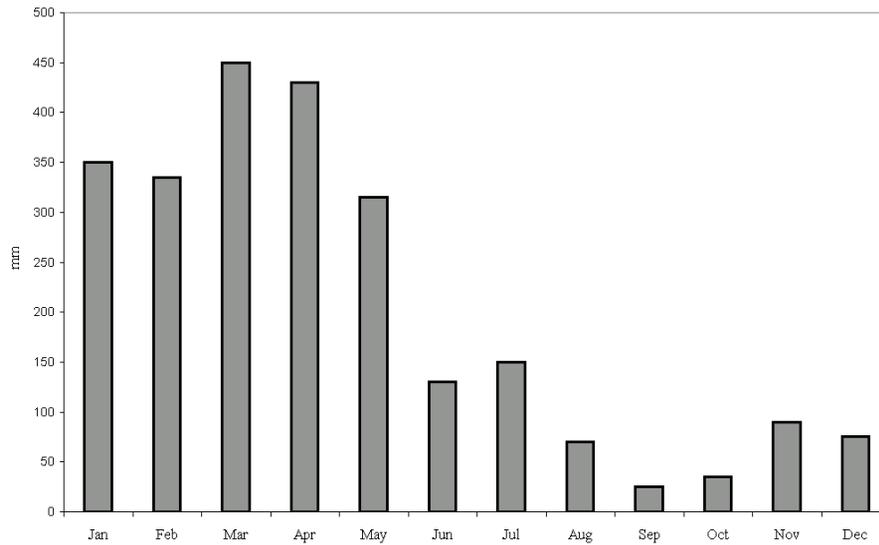
Fig. 3. Average annual precipitation (mm) in Curuai floodplain (from Agência Nacional de Águas-ANA).
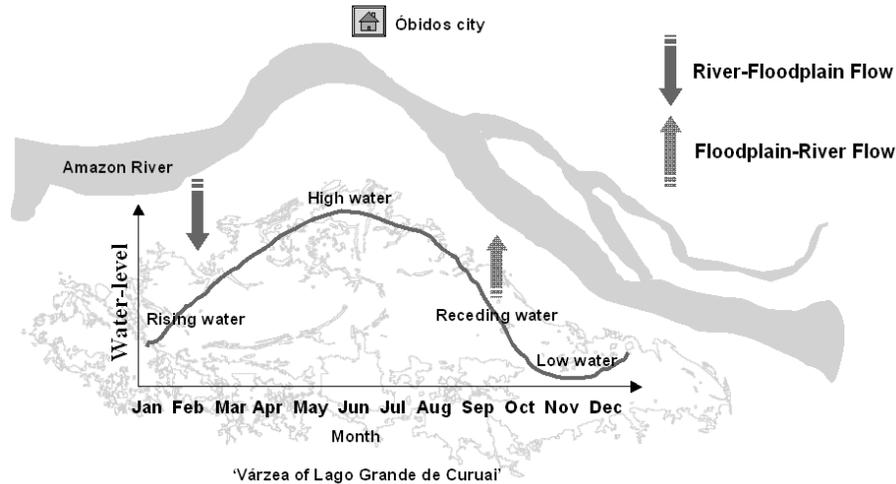
Fig. 4. Theoretical water level dynamics at Curuai Floodplain.
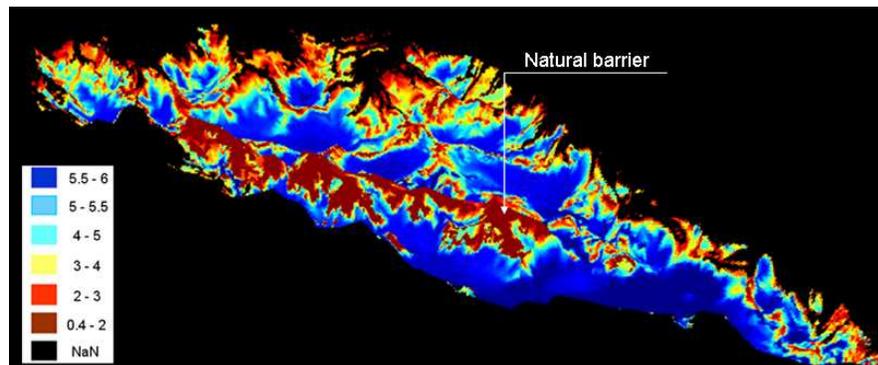
Fig. 5. Curuai floodplain bathymetry in meters (from Barbosa, 2005).
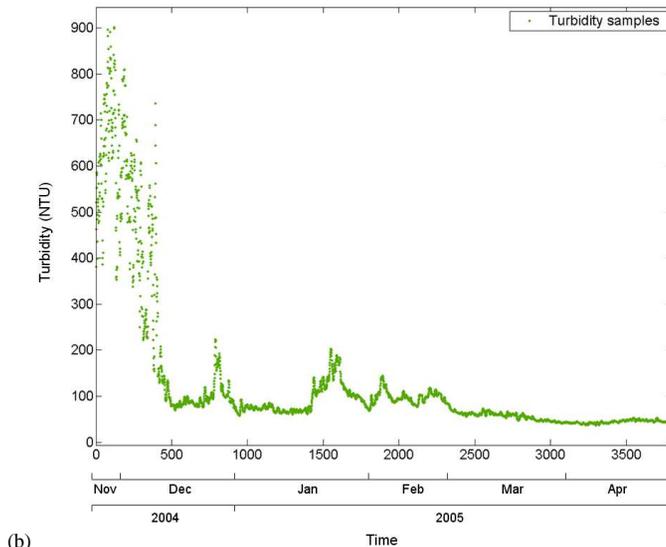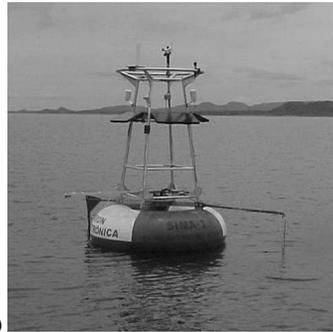
Full Screen / Esc

Fig. 6. (a) Photo of SIMA installed at "Lago Grande" in Curuai floodplain (see Fig. 1 for location); **(b)** time series of turbidity (NTU) collected by SIMA.
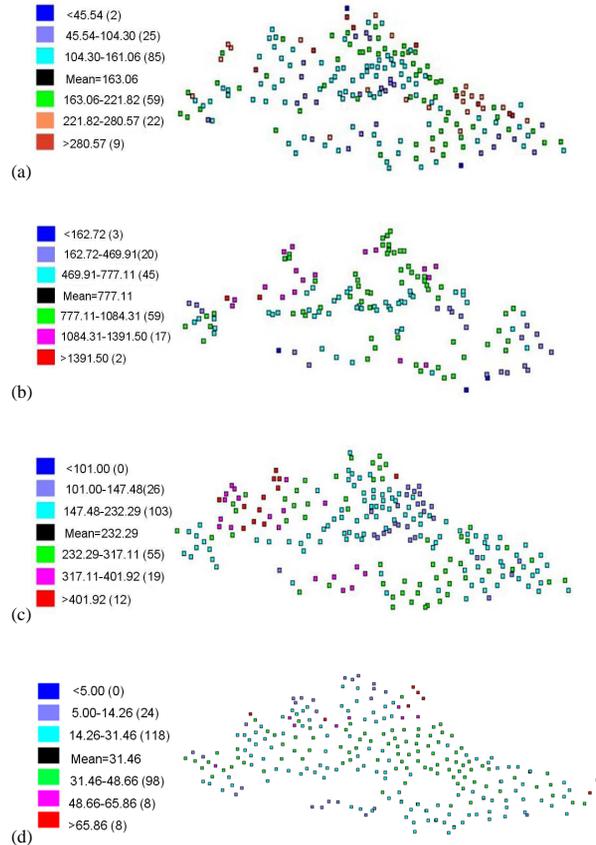
Fig. 7. Turbidity samples distribution grouped by standard deviation bins (the numbers between parenthesis indicate the amount of samples that possess one clustering standard deviation): **(a)** receding water level, **(b)** low water level, **(c)** rising water level and **(d)** high water level.

Full Screen / Esc

Printer-friendly Version

Interactive Discussion
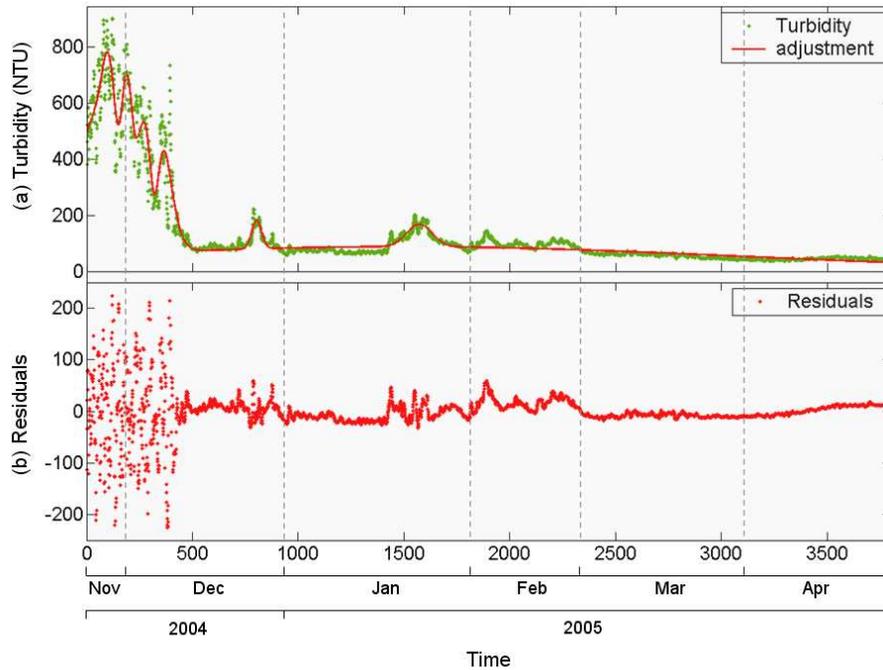
Fig. 8. Fitting the turbidity time series using eight-term Gaussian series.
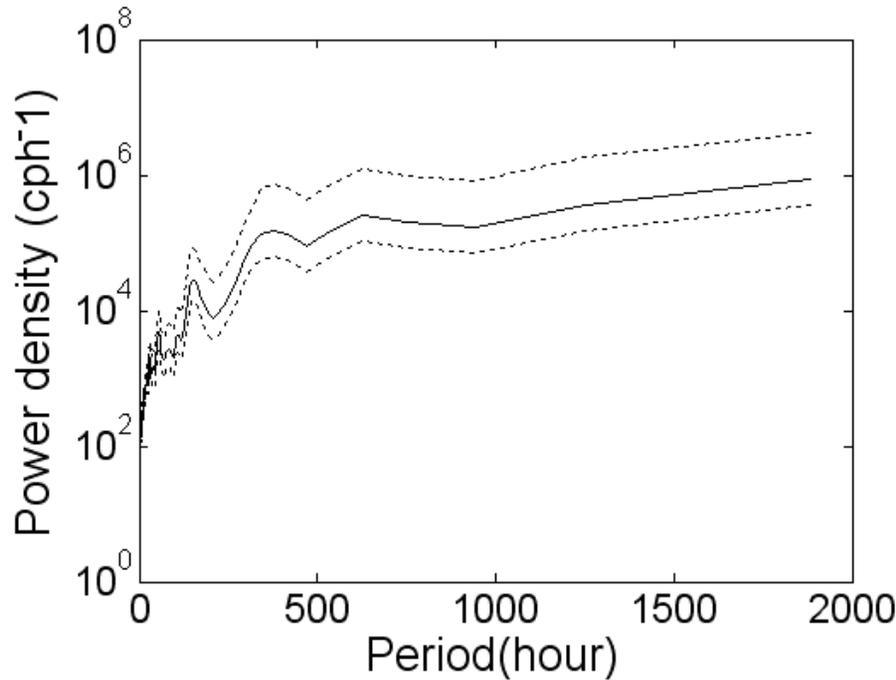
Fig. 9. Fourier power spectrum of turbidity time series. The dashed lines represent the confidence intervals limits.
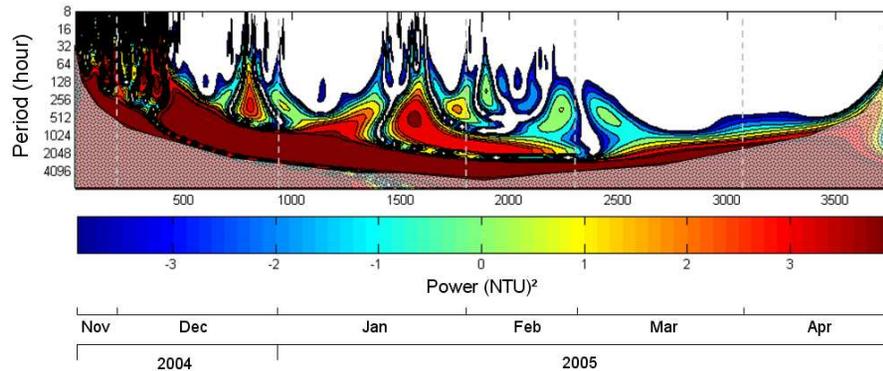
Fig. 10. Wavelet analysis of turbidity time series. Cross-hatched regions on either end indicate the "cone of influence", where edge effects become important.

Printer-friendly Version

Interactive Discussion
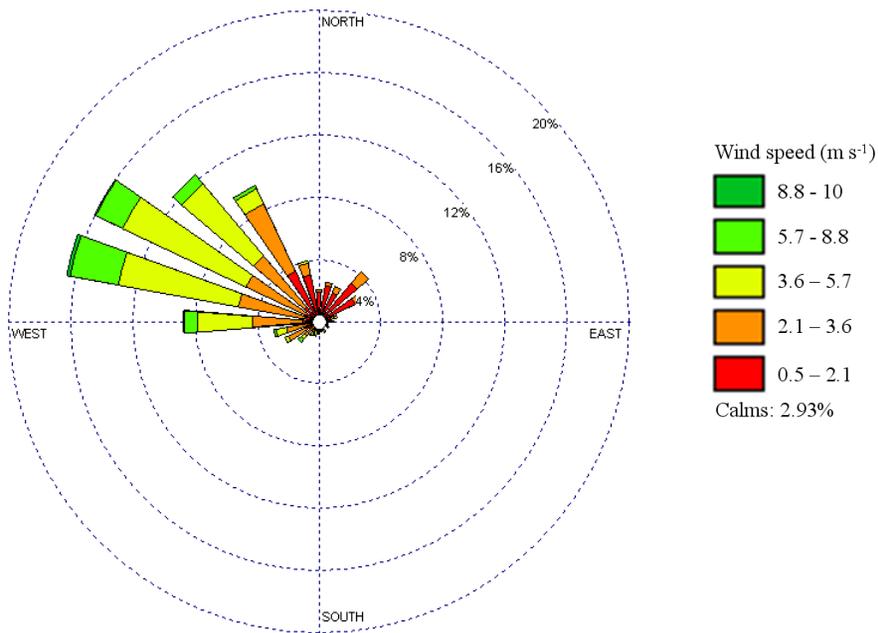
Fig. 11. Wind rose diagram of data collected by SIMA from 20 November 2004 to 3 April 2005.

(a)

(b)

(c)
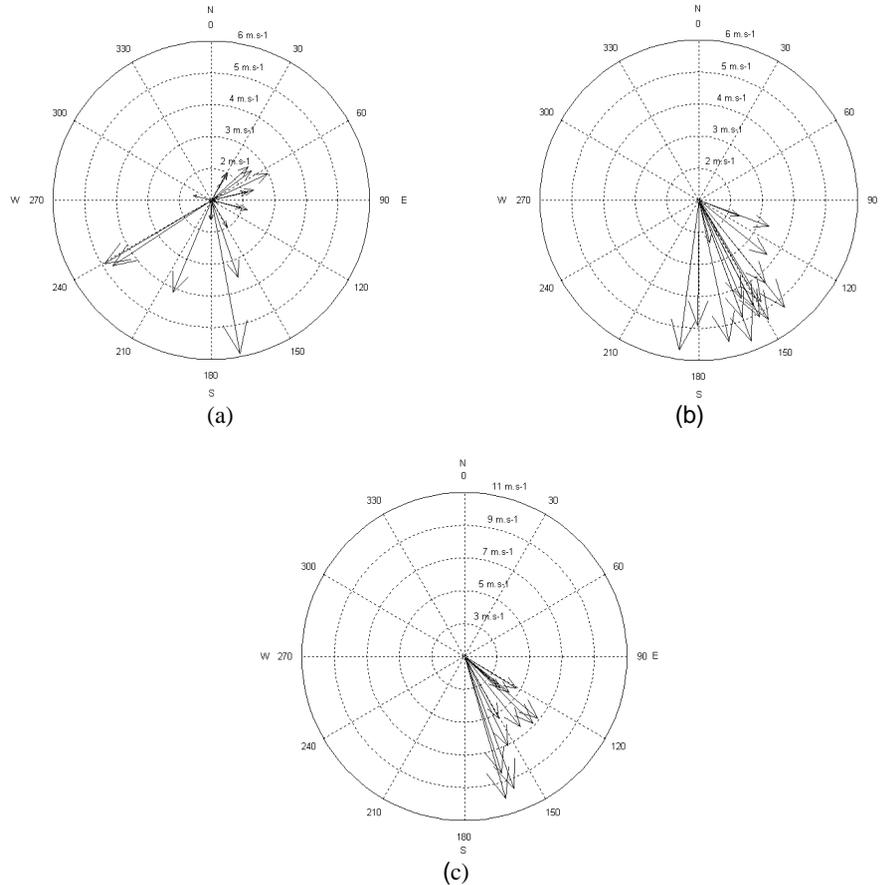
Fig. 12. Compass wind roses of events E1 **(a)**, E2 **(b)** and E3 **(c)**.
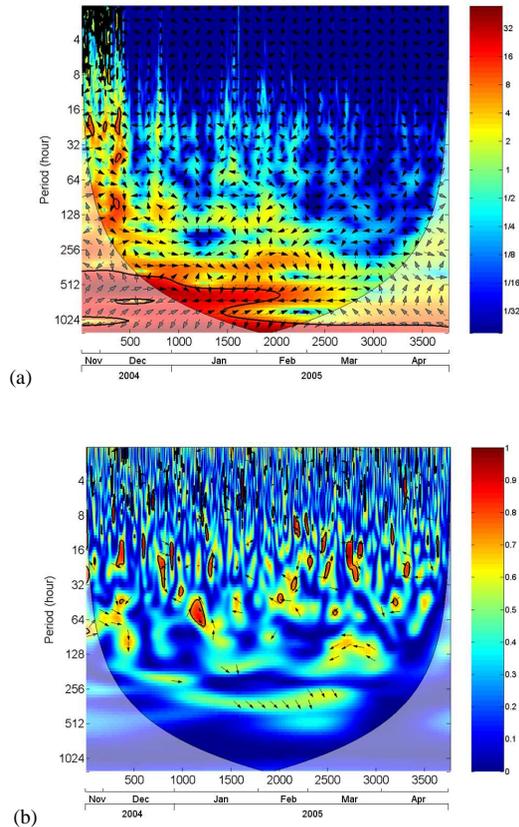
Fig. 13. (a) Cross wavelet transform of the standardized turbidity and wind intensity time series. The 5% significance level against red noise is shown as a thick contour. The relative phase relationship is shown as arrows; **(b)** Squared wavelet coherence between the standardized turbidity and wind intensity time series. The 5% significance level against red noise is shown as a thick contour.
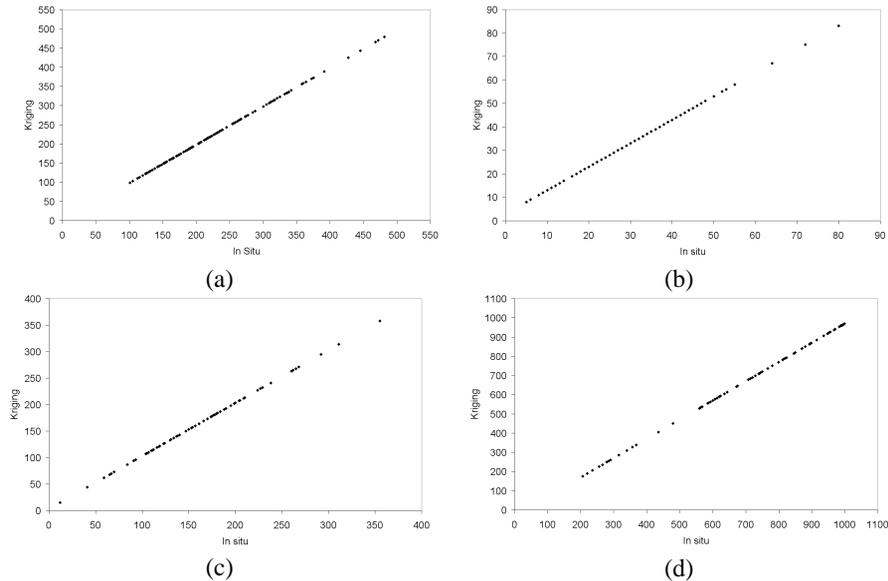
Fig. 14. Performance of each interpolated turbidity data: **(a)** during rising water level, **(b)** during high water level, **(c)** during receding water level and **(d)** during low water level.
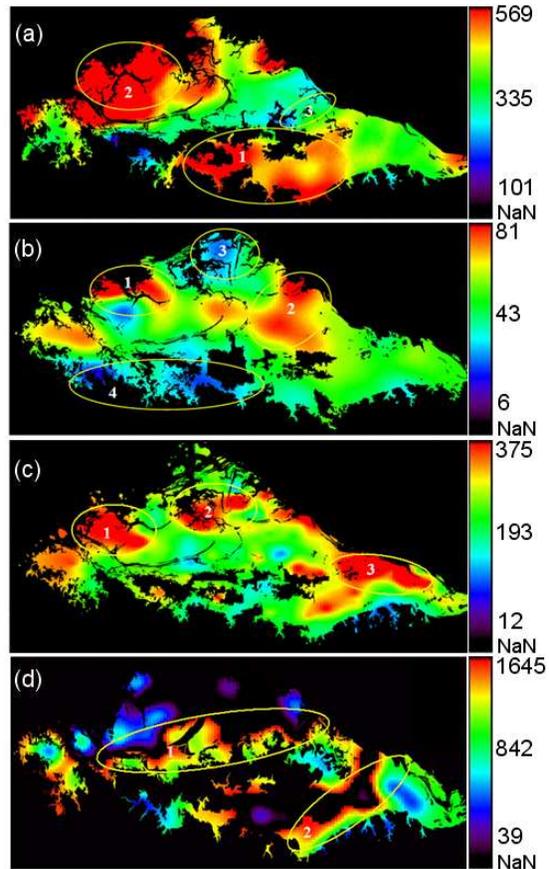
Fig. 15. Ordinary kriging maps: **(a)** turbidity distribution (NTU) during rising water level, **(b)** during high water level, **(c)** during receding water level and **(d)** during low water level.